AIP | Physics of Fluids

Pulsatile flow past an oscillating cylinder

Adnan Qamar, Robinson Seda, and Joseph L. Bull

Citation: Phys. Fluids **23**, 041903 (2011); doi: 10.1063/1.3576186
View online: http://dx.doi.org/10.1063/1.3576186
View Table of Contents: http://pof.aip.org/resource/1/PHFLE6/v23/i4
Published by the AIP Publishing LLC.

Pulsatile flow past an oscillating cylinder

Adnan Qamar, Robinson Seda, and Joseph L. Bull[a)]
Department of Biomedical Engineering, University of Michigan, Ann Arbor, Michigan 48109, USA

(Received 19 August 2010; accepted 25 February 2011; published online 21 April 2011)

A fundamental study to characterize the flow around an oscillating cylinder in a pulsatile flow environment is investigated. This work is motivated by a new proposed design of the total artificial lung (TAL), which is envisioned to provide better gas exchange. The Navier–Stokes computations in a moving frame of reference were performed to compute the dynamic flow field surrounding the cylinder. Cylinder oscillations and pulsatile free-stream velocity were represented by two sinusoidal waves with amplitudes A and B and frequencies ω_c and ω, respectively. The Keulegan–Carpenter number ($K_c=U_o/D\omega_c$) was used to describe the frequency of the oscillating cylinder while the pulsatile free-stream velocity was fixed by imposing $\omega/K_c=1$ for all cases investigated. The parameters of interest and their values were amplitude ($0.5D<A<D$), the Keulegan–Carpenter number ($0.33<K_c<1$), and the Reynolds number ($5<Re<20$) corresponding to operating conditions of the TAL. It was observed that an increase in amplitude and a decrease in K_c are associated with an increase in vorticity (up to 246%) for every Re suggesting that mixing could be enhanced by the proposed TAL design. The drag coefficient was found to decrease for higher amplitudes and lower K_c for all cases investigated. In some cases the drag coefficient values were found to be lower than the stationary cylinder values ($A=0.5$, $K_c=0.3$, and $Re=10$ and 20). A *lock-in* phenomenon (cylinder oscillating frequency matched the vortex shedding frequency) was found when $K_c=1$ for all cases. This lock-in condition was attributed to be the cause of the rise in drag observed in that operating regime. For optimal performance of the modified TAL design it is recommended to operate the device at higher fiber oscillation amplitudes and lower K_c (avoiding the lock-in regime). © *2011 American Institute of Physics*. [doi:10.1063/1.3576186]

I. INTRODUCTION

Obstructive lung disease, including asthma, pulmonary fibrosis, and chronic obstructive lung disease, is one of the leading causes of morbidity and mortality in United States.[1,2] For end-stage lung diseases lung transplant is the only option.[3] As the wait time for the lung availability has increased over the years due to a shortage of donors, several other alternatives have been proposed,[4] which can be labor intensive, costly, and nonambulatory.[5] The need for the development of a total artificial lung (TAL) capable of providing ambulatory total respiratory support for weeks to months has gained interest in recent years.[6] The goal of this device is to serve as a bridge to lung transplant or lung recovery. The TAL is composed of hundreds of microporous hollow fibers (300 μm in diameter) inside an oval shaped cross-sectional casing with inlet and outlet ports for blood and oxygen.[7] The device is attached to the cardiovascular circulation through the pulmonary artery either in parallel or series.[7] When deoxygenated blood enters the device it flows across the bundle of fibers through which oxygen-rich air flows. This cross-flow system allows gas exchange, which is typically governed by the resulting vortex interaction downstream of the cylindrical fibers. Results from initial *in vivo* experiments indicate that the TAL can sustain O_2 and CO_2 requirements for periods as long as seven days in pigs and sheep.[8] Nevertheless, further improvement in the design of the TAL is required to support the basal gas exchange in humans (240 ml/min of O_2 and 200 ml/min of CO_2 for a cardiac output of 4–6 l/min).

The gas exchange process in the TAL is governed by the evolving vortex field behind the cylindrical hollow fibers, and consequently much of the recent research effort has focused on understanding the fluid dynamics interactions associated with the current TAL design under varying operating conditions. Lin *et al.*[9] conducted experimental studies to characterize the vortex evolution behind single and multiple cylindrical fibers under physiological pulsatile flow conditions (Reynolds number $Re=1-5$ and Stokes number $St=0.18-0.37$). For a single cylinder under pulsatile flow, a critical value of the Stokes (St) number, which favors vortex formation, was observed. It was shown that the arrangement of the fibers (side by side, tandem circular, and staggered) plays an important role in the vortex structure behind the fibers with a side-by-side configuration producing larger vortices compared to the other two configurations.

Chan *et al.*[10] investigated, through numerical computations, pulsatile flow and gas transport of a Newtonian passive fluid across an array of cylindrical microfibers. Improvement in gas exchange was found to be significant when the pulsatile oscillation frequency and Reynolds number were increased while keeping a small void fraction between the fibers. The staggered array arrangement was shown to give better gas transfer per fiber (for relatively large void fraction) and a smaller pressure drop (low drag). Zierenberg *et al.*[11,12]

[a)]Author to whom correspondence should be addressed. Electronic mail: joebull@umich.edu; Telephone: 734 647–5395; Fax: 734 647–4834.

performed computational studies where the effect of pulsatility on the drag and the gas exchange on a single fiber were investigated for Newtonian and non-Newtonian fluids. For single fiber they found that the drag force increases with increasing Re and amplitude and frequency of the pulsatile flow. The value of the Sherwood number (Sh) was always lower than that for the steady-state value, which indicates that no improvement was achieved due to pulsatility. It was concluded that for the maximum mass transport across the fiber, the device should be operated close to steady state.

Physiological conditions in the human body do not allow for operating the TAL close to steady state since the heart rate and cardiac output will dictate frequency and amplitude, respectively. Thus, the TAL design needs to be reconsidered. An optimal design of an artificial lung device must provide complete gas exchange support, should match the native pulmonary impedance to prevent right ventricular dysfunction,[13] should have small flow resistance (flow drag), should cause minimal blood trauma, and should be compact in size for ambulatory purposes. From a fluid mechanics point of view, in order to improve the gas exchange in the TAL, mixing needs to be enhanced or more specifically the vorticity production inside the device should be increased. Since pulsatility alone cannot be used to increase the vorticity production,[11,12] a simple mechanical way should be thought off, keeping in mind the constraints associated with the design of the TAL. A proposed modification is to provide a mechanical *oscillation to the entire array of microfibers*, which could provide additional convective forces to the fluid in the direction normal to the direction of the vibration. This could potentially result in enhancing the vorticity and in turn the gas exchange associated with the basic TAL design with possibly minimal increase in drag. Since the amplitude and frequency of the oscillations will be small, the associated blood cell trauma which is caused by shearing of the blood (caused by pumping blood in mechanical ventilators) is envisioned to be minimal as no high shear stresses would be generated via this approach. Also, if the induced stress field via the cylinder oscillation does not activate the platelets, it could potentially help in reducing the chances of blood clotting and infections as the fibers are under constant motion.

To better understand the fluid dynamic interaction associated with cylinder oscillation in pulsatile flow a detailed parametric investigation is required. Many studies[14,15] for forced and free cylinder oscillation for uniform flows are available in the literature. Since these studies were primarily focused on structural and marine application, low Reynolds number cases were ($Re < 100$) rarely investigated. However, from these studies it can be inferred that when a cylindrical body undergoes oscillation in a uniform stream of fluid[16,17] or when a fixed body is exposed to a stream with an imposed oscillation,[18] the structures of unsteady separation are altered dramatically. These oscillations provide a means to couple the flow along the span of the body, and this usually results in a large increase in the surface vorticity and correlation length. Detailed analysis of the flow reveals that the motion of the body in uniform flow can take control of the instability mechanism that can lead to vortex shedding at much lower Reynolds number ($Re < 14$).[19] Hence, the flow generated by vortex shedding around a vibrating cylindrical body can have very significant differences from that around a fixed one. Moreover, the combination of pulsatile/oscillatory flow with forced cylinder oscillation would further result in altering the fluid dynamics significantly.

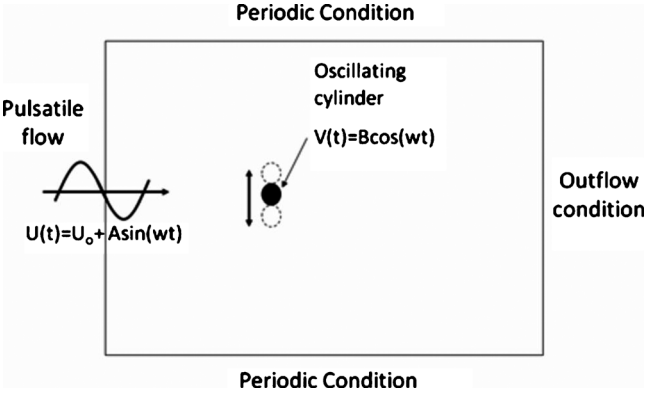

FIG. 1. Schematic of pulsatile flow past the oscillating cylinder.

As no previous studies have been reported for this fundamental class of fluid mechanics problem involving *cylinder oscillation* under *pulsatile flow* environment, it is the purpose of this study to fill this void. This work, motivated by the TAL, is focused on elucidating flow characterization around a single oscillating cylinder under pulsatile inflow conditions. Although the influence of neighboring fibers is not taken into account, this fundamental study represents the first step of a series of studies as it represents the basic element of the TAL device. In subsequent work, the influence of neighboring fiber oscillations will be considered to better characterize the device. The present work deals mainly with a detailed numerical investigation of the oscillating cylinder interaction with the incoming pulsatile flow for various oscillation amplitudes and frequencies. As the motivation of this study is the TAL, the present study explores the parametric space for low Reynolds number cases ($Re < 20$), which corresponds to the TAL operating conditions.

The following work describes a fundamental fluid mechanics problem solved numerically for various oscillation amplitudes and frequencies (Secs. II–IV). The results from a stationary cylinder are presented first and compared to those for an oscillating cylinder (Sec. V). Streamline evolution in time, vorticity, and drag are used to compare the effects of the different degrees of oscillation. Finally, conclusions and recommendations are presented in Sec. VI.

II. PROBLEM STATEMENT

Numerical computations of the pulsatile flow past an oscillating cylindrical fiber have been investigated in the present study. A schematic of the problem is shown in Fig. 1. A Newtonian fluid with constant density ρ and viscosity μ is assumed. An infinitely long horizontal cylindrical fiber with diameter D which is placed perpendicular to the incoming pulsatile flow in x-direction is considered. The pulsatile free-stream velocity profile is given by

$$U_\infty = U_o + B\sin(\omega t), \tag{1}$$

where U_o is the mean average velocity, B is the dimensional amplitude of velocity oscillation, ω is the dimensional angular frequency of the oscillation, and "t" is the dimensional time. The cylinder is allowed to oscillate only in vertical direction and the cylinder vibrating velocity is given by

$$U_c = A\sin(\omega_c t), \tag{2}$$

where A is the dimensional oscillating velocity amplitude and ω_c is the dimensional frequency of oscillation of the cylinder.

III. GOVERNING EQUATIONS

The evolution of the flow field due to the oscillation of the cylindrical fiber is governed by the unsteady Navier–Stokes equations in a moving frame of reference. For the incompressible fluid surrounding the cylinder, the conservation of mass and momentum on an arbitrary control volume (CV) Ω, whose boundaries are moving with time, is given by

$$\frac{\partial}{\partial t^*}\int_\Omega \rho d\Omega^* + \int_S \rho(\vec{V}^* - \vec{V}_s^*)\cdot \hat{n} ds^* = 0, \tag{3}$$

$$\frac{\partial}{\partial t^*}\int_\Omega u_i^* d\Omega^* + \int_S [u_i^*(\vec{V}^* - \vec{V}_s^*)]\cdot \hat{n} ds^* = -\int_S p^* \hat{i}_i \cdot \hat{n} ds^* + \frac{1}{Re}\int_S \nabla u_i^* \cdot \hat{n} ds^*, \tag{4}$$

where Ω^* is the nondimensional volume, ρ represents the density, p^* is the nondimensional pressure, $\vec{V}^*$ is the flow nondimensional velocity vector, u_i^* is the ith nondimensional velocity component, $\hat{i}$ is the respective unit vector in the Cartesian system, Re is the Reynolds number ($Re = \rho U_o D/\mu$) based on the cylinder diameter, and $\vec{V}_s^*$ is the nondimensional grid velocity of the moving boundary of the control volume. Due to the moving coordinate system, which involves control volume with moving boundaries ($\vec{V}_s^* \neq 0$), an additional equation which is an outcome of a typical control volume formulation has to be satisfied simultaneously with the above conservation equations. This equation relates the change of the elementary control volume to the coordinate frame velocity and is referred to as space conservation law (SCL),[20]

$$\frac{\partial}{\partial t^*}\int_\Omega d\Omega^* + \int_S \vec{V}_s^* \cdot ds^* = 0. \tag{5}$$

This SCL describes the conservation of space when the control volume changes its shape or position with time.

The scales used to nondimensionalize the governing equation are

$$u^* = \frac{u}{U_o}, \quad v^* = \frac{v}{U_o}, \quad t^* = \frac{t}{D/U_o}, \quad x^* = \frac{x}{D}, \quad y^* = \frac{y}{D}, \quad p^* = \frac{p}{\rho U_o^2}, \quad \text{and} \quad \omega^* = \frac{\omega}{\omega_c}. \tag{6}$$

The above system of conservation laws is solved subject to the boundary conditions depicted in Fig. 1. A pulsatile inflow velocity [Eq. (1)] is imposed at the inlet. At the oscillating cylinder surface no-slip condition is imposed, which implies that the fluid in contact with the cylinder surface also has the same velocity as that of the cylinder [Eq. (2)]. The inflow pulsatile velocity and the cylinder oscillating velocity are nondimensionalized using the above scales to yield

$$U_\infty^* = 1 + B^*\sin(\omega^* t^*/K_c) \tag{7}$$

and

$$U_c^* = A^*\sin(t^*/K_c), \tag{8}$$

where K_c is the Keulegan–Carpenter number ($K_c = U_o/D\omega_c$) and A^* and B^* are the dimensionless velocity amplitudes. The exit is modeled as a free outflow[21] that is placed a sufficiently large distance from the cylinder surface. The top and bottom of the computational domain are modeled as a periodic boundary condition. Thus, for every time step the evolving flow field due to the oscillating cylinder inside a pulsatile flow is solved using the conservation equations [Eqs. (3) and (4)] along with the above mentioned boundary conditions.

IV. NUMERICAL PROCEDURE

In order to obtain a discrete form of the conservation laws, the solution domain is discretized into a finite number of unstructured quadrilateral CVs. The computational points (nodes) are placed at the center of each CV, while boundary nodes reside at the center of boundary cell faces. For the time discretization, a fully implicit time differencing is employed. All dependent variables are stored in a collocated variable arrangement, which allows only one set of control volumes to be generated, as opposed to four sets in the case of staggered arrangement.

In the present computations, the grid velocities are not explicitly computed from the SCL; however, the volume flux through the CV faces, which results from its motion, is calculated using Eq. (5) as

$$\sum_{j=1}^{m}\int_{s_i} \vec{V}^* \cdot \hat{n} ds^* = \frac{\Omega_P^{n*} - \Omega_P^{n-1*}}{\delta t_n^*} = \sum_{j=1}^{m}\frac{\delta\Omega_j^*}{\delta t_n^*}, \tag{9}$$

where $\delta\Omega_j^*$ is the volume swept by the cell face S_j during the time interval $\delta t_n^* = t_n^* - t_{n-1}^*$. The swept volume $\delta\Omega_j^*$ is easily computed since the CV vertices are known for all times. The convective term in the momentum equation, which represents the rate at which the dependent variable (u_i^*) is convicted into (out of) CV through cell face "S," is approximated as follows:

$$C_j = \int_{s_j} u_i^*(\vec{V}^* - \vec{V}_s^*) \cdot \hat{n} ds^* \approx \dot{m}_j (u_i^*)_j^{\phi}, \tag{10}$$

$$\dot{m}_j = \int_{s_j} (\vec{V}^* - \vec{V}_s^*) \cdot \hat{n} ds^* \approx \left(\vec{V}_j^{*\phi} \cdot \hat{n} ds^* - \frac{\delta \Omega_j^*}{\delta t_n^*} \right), \tag{11}$$

where the ϕ quantities represent the interpolated values at the cell face S. The cell face velocity $\vec{V}_j^*$ is obtained from a special interpolation procedure as described by Demirdzic and Muzaferija[22] to assure stable solution procedure and to avoid checker-board pressure oscillations associate with collocated grid arrangement. The value of $(u_i^*)_j^{\phi}$ is obtained by a blend of a second-order accurate formula[22] with some small amount of first-order upwinding procedure,[22]

$$(u_i^*)_j^{\phi} = (u_i^*)_j^{FO} + \gamma [(u_i^*)_j^{SO} - (u_i^*)_j^{FO}], \tag{12}$$

where γ is the blend factor with the value between 0 and 1 and the superscripts "FO" and "SO" represent the orders of accuracy. This approach combines the accuracy of a second-order scheme and the stability of a first-order scheme.

The diffusive flux through the cell face j is approximated as

$$D_j = \int_{s_j} \mu \nabla u_i^* \cdot \hat{n} ds^* \approx \mu (\nabla u_i^*)_j^{\phi} \cdot \hat{n} ds^*, \tag{13}$$

$$(\nabla u_i^*)_j^{\phi} = (\nabla u_i^*)_j + \left[\frac{(u_i^*)_{P_j} - (u_i^*)_P}{|d_j|} \frac{s_j}{|s_j|} - \frac{\overline{\nabla u_i^* \cdot \vec{d}_j}}{|d_j|} \frac{s_j}{|s_j|} \right], \tag{14}$$

where the overbar represents the arithmetic mean between the nodes P and P_j across the cell face j and the value of $(\nabla u_i^*)_j$ is calculated using the space-centered second-order formula.[22] This second-order space-centered interpolation cannot sense the oscillations having period twice than the characteristic length of the mesh. Thus, an induced unphysical oscillatory profile remains superimposed onto the otherwise smooth spatial variation of the dependent variable. To avoid this situation a third-order diffusion term [expression in square brackets in Eq. (14)] is introduced. This additional diffusion transport smoothes out these unphysical oscillations during the solution process.

After the discretization of the conservation laws, the system of equations can be assembled in the form of nonlinear algebraic equations which links the value of the dependent variable at the control volume center with its values at the points in the neighborhood as

$$a_{(u_i^*)P} (u_i^*)_P - \sum_{j=1}^{m} a_{(u_i^*)j} (u_i^*)_j = b_{(u_i^*)}. \tag{15}$$

The resulting coefficients can be found in Ref. 22. These coefficients are obtained by utilizing the collocated version of the semi-implicit method for pressure linked equation[23] procedure as given by Demirdzic *et al.*[24] The above system is linearized and the set of equation for each dependent variable is temporarily decoupled by assuming that the coefficients and source term are known (based on previous time step), which results in a system of linear algebraic equation of the form

$$A_{(u_i^*)} (u_i^*) = b_{(u_i^*)} \tag{16}$$

for all the dependent variables. In the present computations the above linear system is solved using the conjugate gradient squared stabilized method,[25] with an incomplete Cholesky preconditioner.

Grid generation at each time step is carried out via a layering approach.[26] The entire solution domain is divided into three layers that surround the oscillating cylinder at any instant. The mesh points in the layer surrounding the moving body (layer 1) move as if they are attached in a rigid manner to the body. The mesh nodes in the third layer are fixed with respect to time. The velocities of the mesh point in second layer are gradually relaxed from their corresponding rigid values through a weight function.[26] The weighting function is designed to gradually reduce the mesh velocities from their rigid values depending on their spatial distance from the edge of the first layer. To improve the aspect ratios in the second layer, an iterative orthogonal Laplacian algorithm[27] was used at each time step.

V. RESULTS AND DISCUSSION

The oscillation of the cylindrical fiber inside the TAL is envisioned to improve the basal gas exchange rate in TAL to ultimately provide total respiratory support. Thus, a parametric study is carried out to understand the fluid dynamics associated with an oscillatory cylinder and to elucidate the role of various parameters for a single cylinder, which might provide insights into the proposed TAL design. The operating range of the TAL corresponds to low Reynolds numbers. As a result the cylinder oscillation is studied for Re=5, 10, and 20 as investigated by other researchers.[9–12] It has been demonstrated by Chan *et al.*[10] that pulsatile flow improves the gas exchange for the "array" of cylindrical microfibers by increasing the Reynolds number and keeping small void fraction between the fibers. However, in single fiber studies[11,12] no improvement in the gas exchange is observed due to pulsatility. From a physiological perspective, the heart acts as natural pump to the TAL and therefore it would be challenging to vary the pulsatility in the TAL. Thus, even though the gas exchange can be enhanced via increasing pulsatility, its practical applicability would be limited. Thus, in the present study the pulsatile inflow [Eq. (7)] is fixed for all the cases investigated with $B^*=0.25$ and $\omega/K_c=1$. Finally, the amplitudes (A^*) of the oscillation of the cylinder [Eq. (8)] are taken to be 0.5 and 1 at $K_c=0.3$ and 0.5 and 1 for each Reynolds number.

To check the robustness and accuracy of the computational approach used in the present study, the solver is first validated against benchmark cases found in the literature. Two cases are used to validate the solver: uniform flow past a fixed cylinder for different Reynolds numbers and uniform flow past an oscillating cylinder under varying frequency ratio of cylinder oscillation. Table I compares the result obtained by the present solver with other studies for lift and drag characteristics. It is concluded that the results obtained

TABLE I. Comparison between the results obtained by the present work and those found in the literature.

Reference	Parameters	Drag coefficient	Lift coefficient
Wanderley and Levi[a] (stationary)	Re=100	1.33	0.163
Present study (stationary)	Re=100	1.33	0.161
Guilmineau and Queutey[b] (oscillating)	Re=185; Frequency Ratio =1.10, 1.12, and 1.20	0.149, 0.128, and 0.095	0.897, 0.807, and 0.963
Present study (oscillating)	Re=185; Frequency Ratio =1.10, 1.12, and 1.20	0.141, 0.111, and 0.090	0.861, 0.810, and 0.972

[a]Reference 28.
[b]Reference 17.

by the numerical procedure utilized in the present study are in good agreement with those found in the literature.[17,28]

For the computations of an oscillating cylinder in pulsatile flow a square computational domain is utilized with the cylindrical fiber placed at the center and all the computational boundaries kept at 30D from the cylinder. The grid and time independence of the results given in the section are confirmed by carrying out the simulations at Re=20, $K_c=0.3$, and $A^*=1$. Three grids (400×400, 450×450, and 500×500) and three time steps ($\Delta t=5\times10^{-4}$, 1×10^{-4}, and 8×10^{-5}) are used to ascertain the grid and time independence. A fine $O(10^{-4})$ nonuniform mesh spacing is used in the region near cylinder surface for resolving the viscous layer, and a coarse $O(10^{-2})$ equally spaced mesh is used in the outer region (near the boundaries of the computational domain), where viscous effects are negligible. The effects of different grids and time steps are observed on the surface drag. It is observed that the difference in surface drag in going from a (450×450) grid to a (500×500) grid is on the order of 1%. So the results are obtained on a (450×450) grid to reduce the computational effort. For this grid the time independence study is carried out, and it is observed that the difference between $\Delta t=1\times10^{-4}$ and $\Delta t=8\times10^{-5}$ is almost less than 2%. Thus, $\Delta t=1\times10^{-4}$ is utilized for all the computations.

A. Pulsatile flow past a stationary cylindrical fiber

In order to assess the improvement in the TAL via the forced fiber oscillation, a baseline solution is first computed for the stationary cylinder at the same pulsatile inflow condition [Eq. (7)]. The flow field evolution across a stationary cylinder in pulsatile flow is first understood and then the associated drag and vorticity magnitude across the cylinder are computed for Re=5, 10, and 20. Figure 2 depicts the streamline profiles at various times in a pulsatile cycle ($B^*=0.25$ and $\omega/K_c=1$) for Re=20. The size of the vortex behind the cylinder is found to be dependent on the pulsatile cycle. At $t>0$ [Fig. 2(a)] two symmetric vortices appear at the back of the cylinder. The growth in the size of the vortices is seen during the inflow fluid acceleration period, $t=\pi/8$-$\pi/2$, [Figs. 3(a)–3(c)] and it continues during the entire inflow deceleration phase $t=\pi/2$-$3\pi/2$. For all the cases investigated (Re=5, 10, and 20) the vortices reach their maximum size at $t=3\pi/2$ [Fig. 3(c)] and remain symmetrically attached to the cylinder. During the last quarter of the pulsatile cycle when incoming fluid starts its acceleration phase again, the vortices start collapsing and are shed. Since the incoming fluid is in acceleration mode it dissipates the shed vortices [Fig. 3(e)] quickly within a short distance (approximately D) from the cylinder. For all the cases a complete dissipation of vortices takes place at around $t=2\pi$, which is the beginning of the new pulsatile cycle. Similar vortex growth and collapse in the last quarter of the pulsatile flow were reported by Lin *et al.*[9] in their fundamental experimental work.

In contrast with the studies of uniform flow past a cylinder,[29] where the size of the vortex increases with the increasing velocity magnitude (Reynolds number), a different trend is observed for the case of pulsatile flow. Maximum vortex size behind the cylinder is observed when the inflow velocity during the cycle reaches its minimum value, while the onset of the vortex occurs just before reaching the maximum velocity. To understand these phenomena pressure gradient across the cylinder was plotted (Fig. 3) for the entire pulsatile cycle. A positive pressure gradient exists behind the cylinder throughout most of the cycle. This adverse pressure gradient causes flow separation and ultimately vortex formation behind the cylinder. As the velocity increases, pressure builds up on the back of the cylinder until it is strong enough to produce flow separation. Soon after the velocity starts to slow down, this pressure gradient reaches a maximum. The vortex continues to increase in size until a favorable pressure gradient is encountered. This event occurs near $t=3\pi/2$, where the velocity is minimum. This favorable pressure gradient is quickly overcome by the increasing momentum of the rushing fluid, which sheds the vortices away from the cylinder surface and subsequently collapses them at the beginning of the new cycle.

The resistance (drag) offered by the TAL needs to be estimated in order to account for the amount of force the heart has to work against. Ideally for the TAL it is desired to have low drag and high gas exchange rate. Therefore, to qualitatively asses these parameters, drag coefficient (C_D) and average vorticity were calculated as means to quantify the degree of gas exchange (mixing) and the resistance inside the TAL, respectively. For the stationary single cylinder case it was found that vorticity (and vortex size) increased with

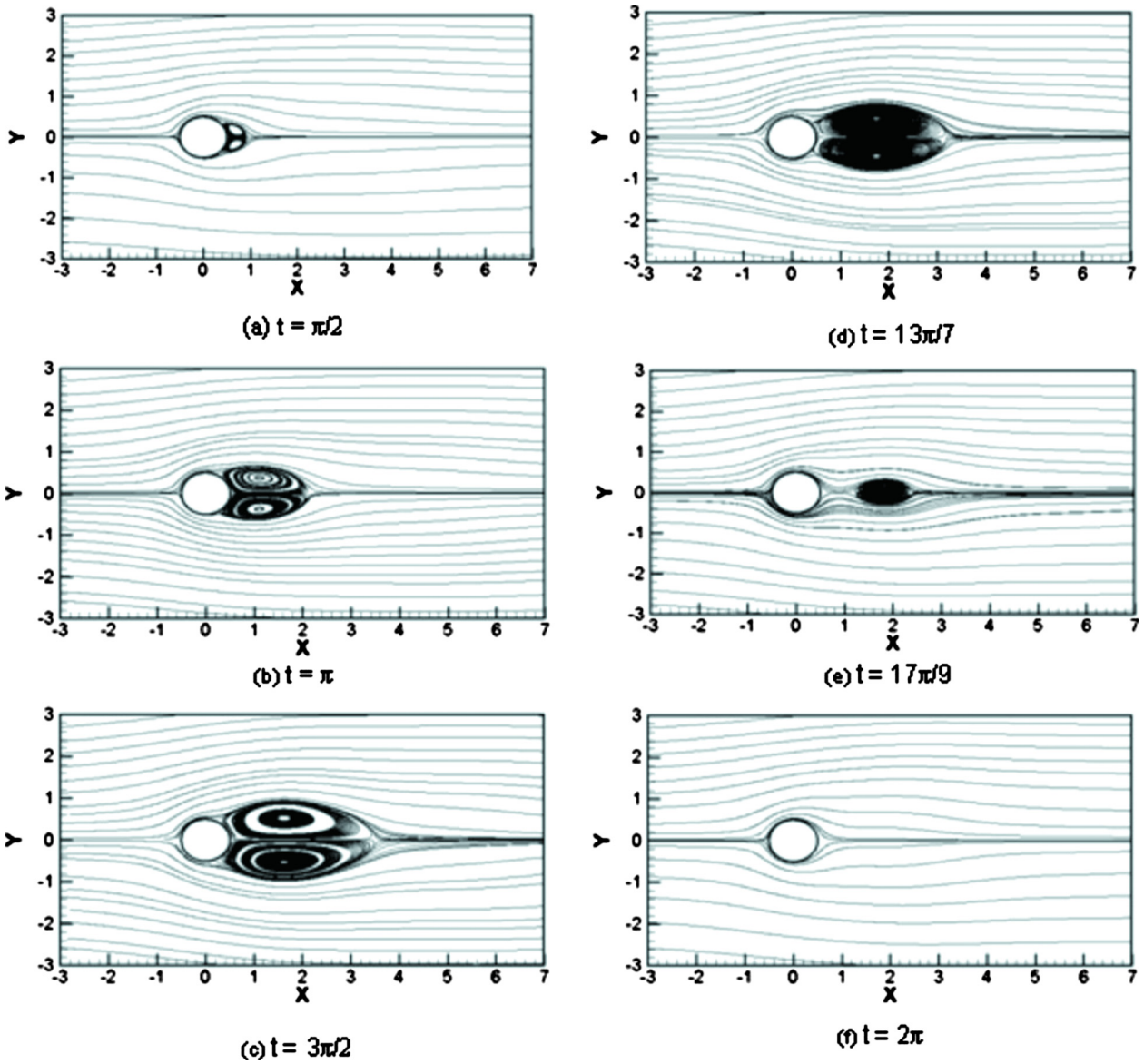

FIG. 2. (Color online) Streamline at various times during a pulsatile cycle ($B^*=0.25$ and $\omega/K_c=1$) for a stationary cylinder at Re=20.

increasing Reynolds number, while C_D followed an opposite trend (see Sec. V B). These two results were also observed in similar studies by Zierenberg *et al.*[11,12]

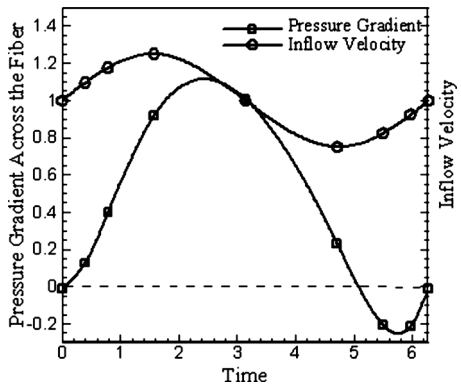

FIG. 3. Temporal pressure gradient across the fiber and the inflow velocity for a stationary fiber.

B. Pulsatile flow past an oscillating cylindrical fiber

The dynamically evolving flow field due to the cylinder oscillation under pulsatile flow is investigated by studying the streamline patterns at various times in the pulsatile cycle. These streamlines can be seen in Fig. 4 for different times in a pulsatile cycle for Re=20, $K_c=0.5$, and $A^*=1$. The K_c value of 0.5 corresponds to two cylinder oscillation cycles per single pulsatile cycle. During the first phase of the cycle ($0\leq t\leq \pi/4$) when the cylinder starts its upward motion from its mean datum location, which also corresponds to fluid acceleration regime of the incoming pulsatile flow, two weak small vortices appear [Fig. 4(a)] on either side of the cylinder. As the cylinder continues its upward motion, the small vortex on the upstream side collapses while being in contact with the cylinder. The vortex on the downstream side detaches from the surface and starts collapsing at a short distance from the cylinder surface [Fig. 4(b)]. Meanwhile, the cylinder reaches its maximum positive amplitude and

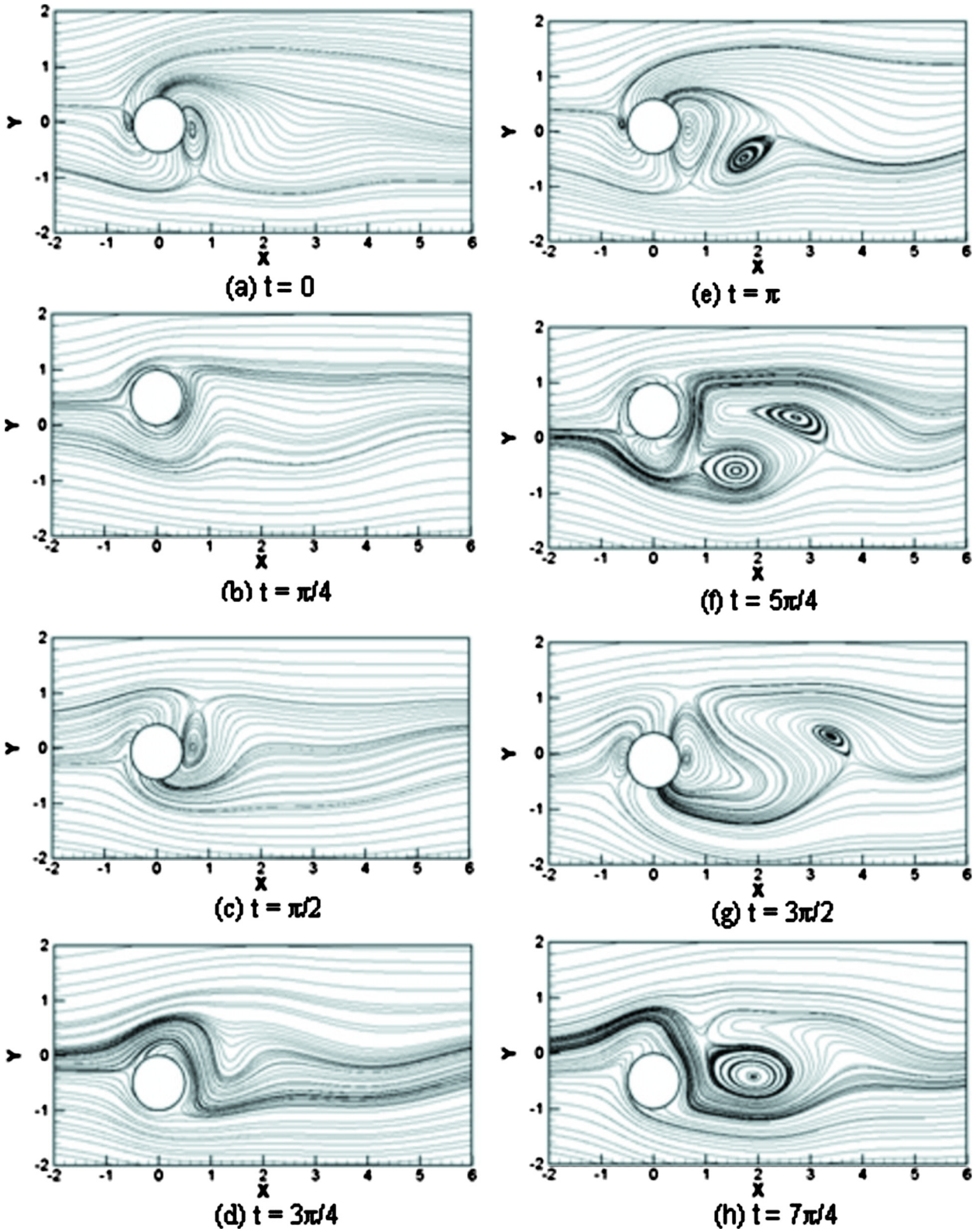

FIG. 4. (Color online) Streamline at various times during a pulsatile cycle for an oscillating cylinder at Re=20, K_c=0.5, and A^*=1.

starts its downward descent. As the cylinder moves downward, a further low pressure region is created downstream of the cylinder resulting in a reappearance of the vortex which had almost collapsed [Fig. 4(c)]. As the cylinder moves down to its minimum displacement [Fig. 4(d)], this vortex is shed and a new vortex appears on the cylinder surface while returning to the mean datum location [Fig. 4(e)]. As the cylinder starts its second cycle of oscillation, the detached vortex in the fluid undergoes a clockwise rotation toward the cylinder while entraining fluid, which results in growth of the vortex. When the cylinder reaches its maximum displacement [Fig. 4(f)] again, the growing attached vortex is shed in

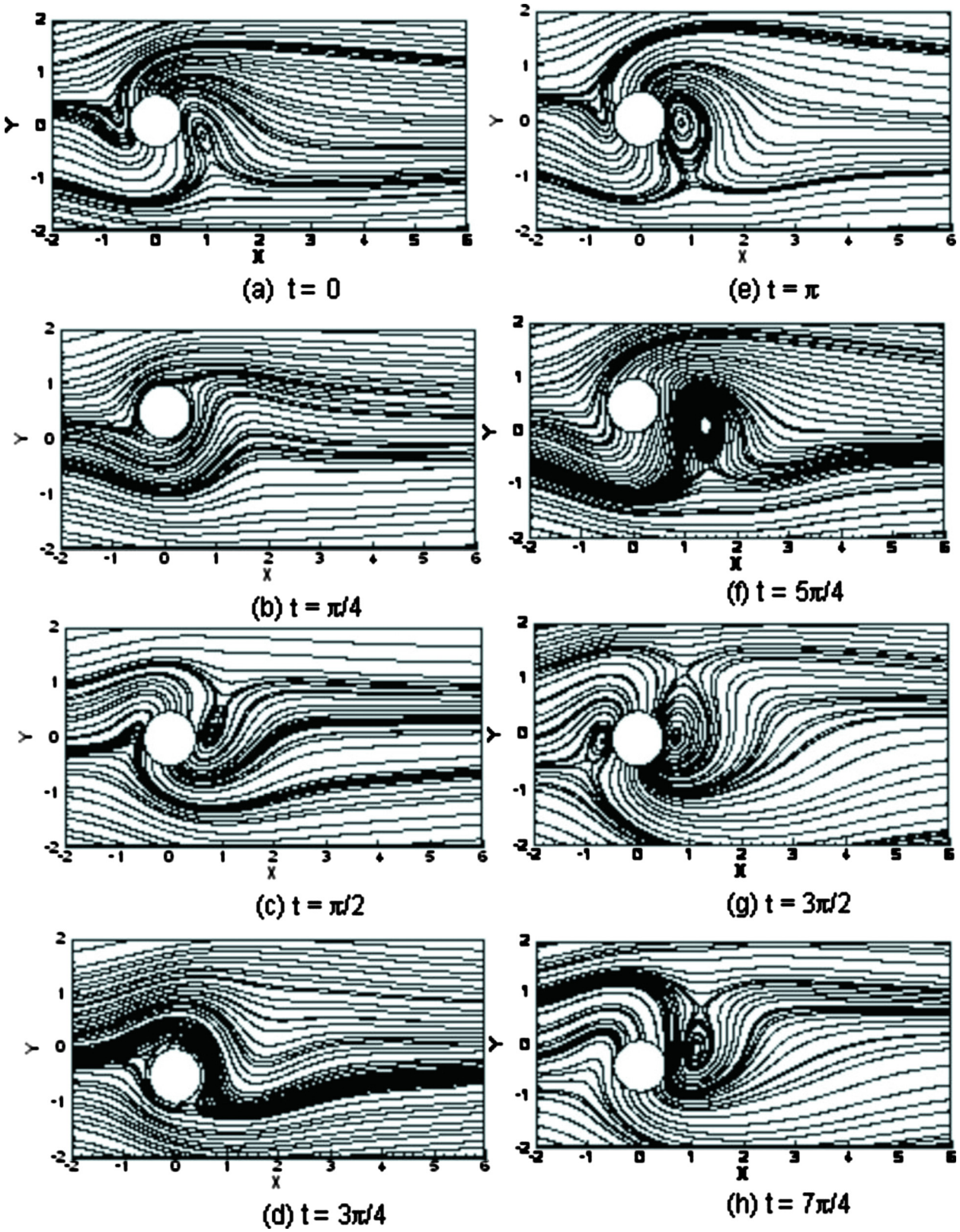

FIG. 5. (Color online) Streamline at various times during a pulsatile cycle for an oscillating cylinder at Re=5, K_c=0.5, and A^*=1.

the fluid, whereas a new vortex starts appearing in the descent mode. As the cylinder moves toward its datum position the clockwise rotation vortex merges with the newly evolving vortex at the surface [Fig. 4(g)]. As a result of vortex merging, the size of the vortex becomes larger and is eventually shed by the cylinder in the return stroke [Fig. 4(h)]. This large vortex gets dissipated downstream shortly, and the two vortices again reappear as the cylinder reaches close its end of the second vibration cycle.

The effects of the Reynolds number on the vortex for-

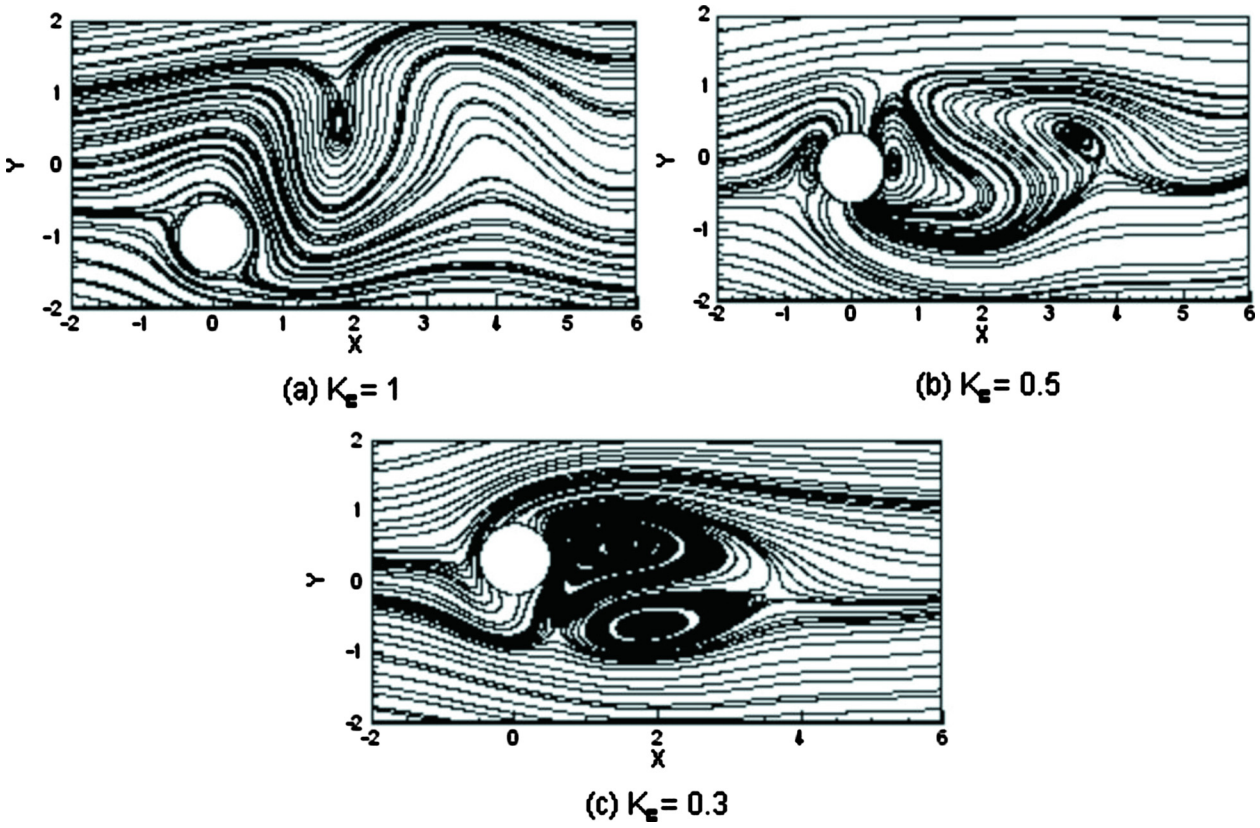

FIG. 6. (Color online) Streamline snapshots at $t=3\pi/2$ for different K_c at Re=20 and $A^*=1$.

mation are also investigated. It is observed that if the cylinder oscillation parameters (A^* and K_c) are kept constant, a similar vortex evolution behavior is observed. Figure 5 shows streamline plots for Re=5, $K_c=0.5$, and $A^*=1$. As the Reynolds number is decreased, the viscous forces associated with the incoming pulsatile flow increase, which are attributed to a quick dissipation of vortices in the downstream side of the cylinder. For the case of Re=5 (Fig. 5) and 20 (Fig. 4), during the first cylinder oscillation cycle the vortex evolution is similar, however, just before the beginning of the second cycle differences is observed. For Re=5 (in contrast to Re =20), the vortices shed during the first cycle are quickly dissipated within a short distance from the cylinder surface resulting in no vortex interaction with vortices of subsequent cycles.

Significant effects of cylinder oscillation frequency and amplitude on vortex formation are found. Figure 6 shows the flow field at $t=3\pi/2$ for Re=20, $A^*=1$, and for different K_c. The values of K_c (1, 0.5, and 0.33) correspond to 1, 2, and 3 oscillations per pulsatile cycle, respectively. It is observed that an increase in the frequency corresponds to the increase in the number of vortices generated per pulsatile cycle. A single vortex is shed when the cylinder returns from its peak location to the datum on either side; thus, in total two vortices are shed per cycle. It can be observed that for $K_c=1$ only one vortex is formed, while for $K_c=0.5$ two vortices are formed. For $K_c=0.33$, only two vortices are observed; however, three vortices were formed (for $t<3\pi/2$). Two of the three vortices combined to form one larger vortex. Although the number of vortices generated is controlled by the cylinder oscillation frequency, for enhancing mixing and gas exchange these vortices need to be convicted downstream, particularly as the TAL has low operating Reynolds numbers. Figure 7 shows the streamlines at $t=3\pi/2$ for Re=20, $K_c=0.5$, and for $A^*=0.5$ and 1. It is observed that an increase in amplitude is associated with an increase in vortex convection downstream of the cylinder. For small amplitude [Fig. 7(a)] the shed vortex is dissipated fast with a distance of two-dimensional downstream of the cylinder, whereas for larger amplitude [Fig. 7(b)] the vortex dissipation takes longer and travels approximately four-dimensional downstream of the cylinder before it completely dissipates. This suggests that both vortex formation and vortex convection/dissipation can be controlled mechanically in the TAL by the frequency and amplitude of the oscillations.

To quantitatively understand the effects of cylinder oscillation in the presence of pulsatile flow, surface quantities (drag and vorticity magnitude) were measured until a periodic steady periodic state is reached. To assess the improvement gained by oscillating the cylinder, results are compared with the cases when the cylinder is not vibrating (Sec. V A). Figure 8 shows the time evolution of drag and surface vorticity magnitude for Re=20 at various cylinder vibrating frequency and amplitudes. A substantial gain in the surface vorticity magnitude across the cylinder is obtained for all the cases investigated whereas no significant gain in the drag values (except for $K_c=1$ for all A^* and Re) is observed. Time average values for vorticity magnitude and surface drag coefficient were computed over one pulsatile cycle. Figure 9 shows the time average values for the vorticity and drag

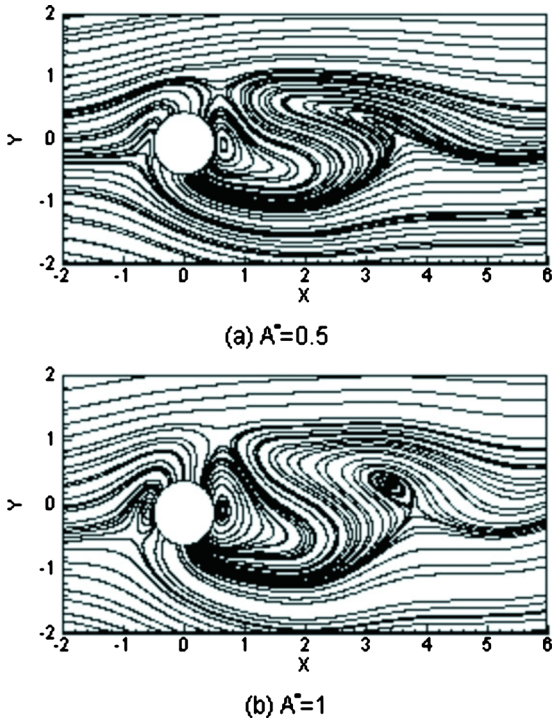

FIG. 7. (Color online) Streamline snapshots at $t=3\pi/2$ for different A at Re=20 and $K_c=0.5$.

coefficient for different amplitudes and frequencies of the cylinder oscillation as a function of Reynolds number. In addition, the drag coefficient and vorticity magnitude for a stationary cylinder are also plotted in the same graph for comparison purposes. For all the cases investigated, the average drag decreases with an increasing Re, whereas surface vorticity magnitude increases with an increasing Reynolds number. These trends are similar to the cases when the cylinder is stationary.

To estimate the improvement obtained by oscillating the cylinder, the percentage increase/decrease in average vorticity magnitude and drag coefficient against the stationary cylinder were calculated and shown in Fig. 10. For a fixed amplitude, decreasing K_c results in a significant gain in vorticity magnitude that corresponds to enhanced mixing and improvement in gas exchange when compared to the case when the cylinders are not oscillating for all Reynolds number. Also, the percentage gain in vorticity is found to be maximum at low Re. This is, in particular, advantageous as the TAL operates in a low Reynolds number regime. It is also noteworthy that a further enormous gain in the vorticity magnitude is seen if the amplitude is doubled under the same conditions. A significant percentage increase in average vorticity of 246% was obtained for $A^*=1$, $K_c=0.3$, and Re=5.

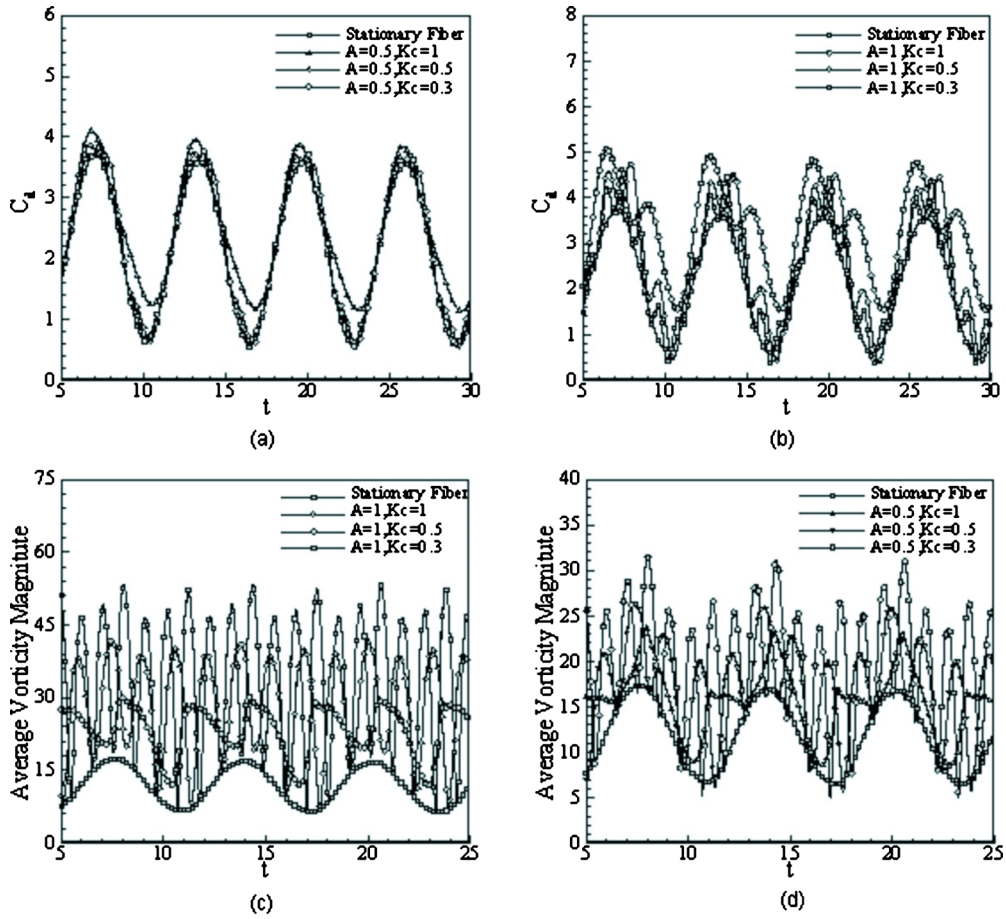

FIG. 8. (Color online) Time evolution of drag coefficient (a) and (b) and average surface vorticity magnitude (c) and (d) for different A^* and K_c at Re =20.

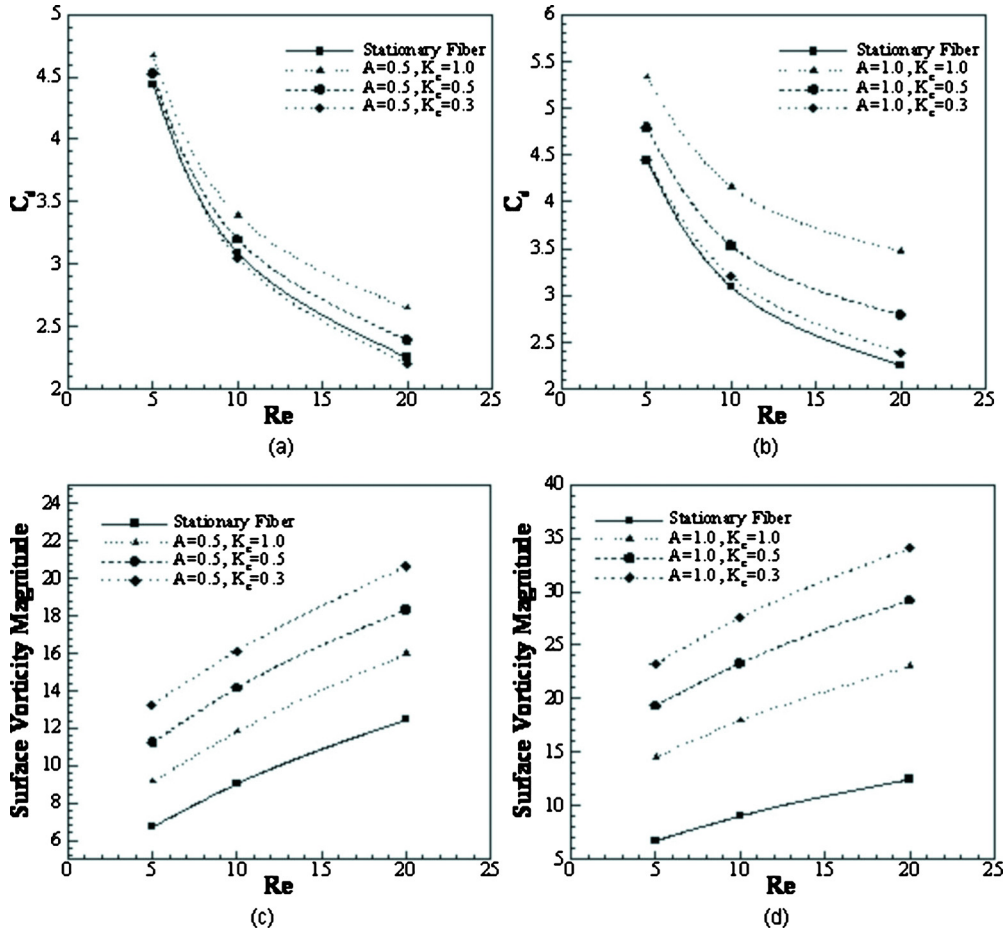

FIG. 9. (Color online) Time average values for drag coefficient (a) and (b) and surface vorticity magnitude (c) and (d) for different A^* and K_c as a function of Re.

This large gain in vorticity is attributed to the associated delay in vortex dissipation via increasing the amplitude of the oscillations.

Although the vorticity magnitude increases with oscillation frequency and amplitude, a reverse trend is seen in the average drag coefficient. For a fixed amplitude, the drag coefficient decreases with a decreasing K_c. Results indicate that there is a considerable increase in average C_D for all Re at $K_c=1$. This sudden jump in the average drag coefficient at $K_c=1$ for all Re is attributed to the *lock-in* condition.[30] This fluid dynamics phenomenon typically occurs when the structure oscillating frequency matches the vortex shedding frequency in the fluid and is associated with sudden increases in drag and lift characteristic of the structure. For all the Reynolds numbers investigated it was confirmed via a fast Fourier transform that for $K_c=1$ the wake shedding frequency matches with the cylinder oscillating frequency. As the K_c value was reduced below 1, the average C_D values decreased further and in some cases ($A^*=0.5$, $K_c=0.3$, and Re=10 and 20) were found to be below the stationary cylinder [Figs. 10(b) and 10(c)] values. This suggests that the proposed TAL design, which includes the cylinder oscillation, should operate in this identified regime (higher oscillation amplitudes and lower K_c) where the gas exchange can potentially be enhanced to the desired limits and the drag associated with the device can be reduced (by increasing oscillation frequency) even below the standard drag values associated with original TAL design (stationary cylinders).

It is important to emphasize that the vortex formation during the case of pulsatile flow past a stationary cylinder results in symmetric vortices that remain attached to the cylinder during most of the pulsatile cycle. In contrast, when an oscillating cylinder is present the events change dramatically. Symmetry is no longer seen, vortices are shed in early stages of the pulsatile cycle, and a dynamic vortex interaction (merging/rotation) is observed. These new interactions associated with the cylinder oscillation may help in improving the gas exchange by increasing the vorticity and reducing the drag in an identified flow regime.

Although the current fundamental study provides new information about pulsatile flow around a single oscillating cylinder, there are limitations to the study and further studies are warranted before applying this potential design modification to the TAL. Increased vorticity production is anticipated to enhance mixing. However, the outcomes of the current study are not sufficient alone to reach conclusions regarding gas exchange enhancement. Future studies involving mass transport are needed to assess the potential improvement in oxygen and carbon dioxide exchange that the modified design would provide. Because the TAL consists of

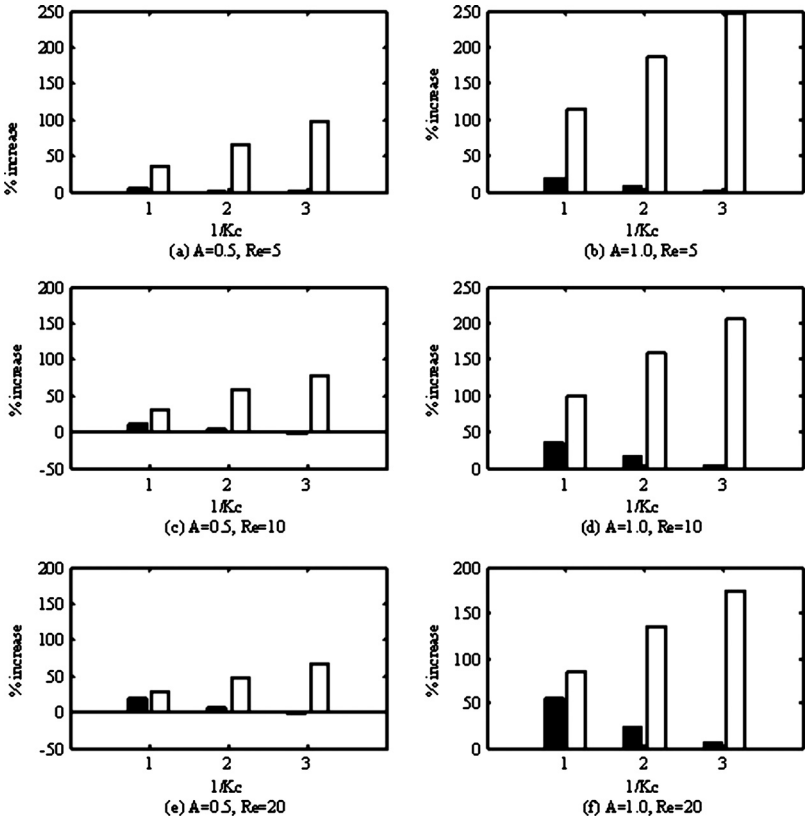

FIG. 10. Percentage increase/decrease in time average drag coefficient (black bars) and surface vorticity magnitude (open bars) against stationary cylinder values for different amplitudes (a) and Re as a function of $1/K_c$.

an array of fibers rather than the single fiber considered in this fundamental study, further investigation of the modified TAL design will also need to consider the combined oscillations of the array of fibers and their interaction to elucidate the role of fiber arrangement in the TAL design. It is important to note that blood exhibits a non-Newtonian behavior due to its composition (plasma and cells), and inclusion of non-Newtonian effects will likely affect the fluid behavior. The potential for platelet activation and hemolysis within the TAL also warrants further investigation.

VI. CONCLUSIONS

Flow characteristics during the oscillation of a fiber in pulsatile flow conditions have been investigated and discussed in the context of the proposed TAL design. Various amplitudes of fiber oscillation and K_c numbers were tested at TAL operating conditions for $Re < 20$. It was found that the number of vortices formed was dependent on the value of K_c while the distance traveled by said vortices was determined by the oscillating amplitude. Lower K_c values and higher oscillating amplitudes promoted vortex formation and shedding suggesting that mixing could be enhanced by mechanically oscillating the fibers contained in the TAL. The drag force was found to decrease for higher amplitudes and lower K_c for every Re. A lock-in condition in which the oscillating fiber frequency matched the vortex shedding frequency was found when $K_c=1$ for all cases, but an optimal operating regime for vorticity enhancement was found when $B^*=1$ and $K_c=0.33$.

ACKNOWLEDGMENTS

This work was supported by NIH Grant Nos. R01HL69420 and R01HL089043.

[1] D. M. Mannino, R. C. Gagnon, T. L. Petty, and E. Lydick, "Obstructive lung disease and low lung function in adults in the United States," Arch. Intern Med. **160**, 1683 (2000).
[2] C. D. Mathers and D. Loncar, "Projections of global mortality and burden of disease from 2002 to 2030," PLoS Med. **3**, 2011–2029 (2006).
[3] A. F. Gelb and R. J. McKenna, "Lung volume reduction surgery update," CHEST **123**, 975–977 (2003).
[4] G. Matheis, "New technologies for respiratory assist," Perfusion **18**, 245 (2003).
[5] F. B. Plötz, A. S. Slutsky, A. J. van Vught, and C. J. Heijnen, "Ventilator-induced lung injury and multiple system organ failure: A critical review of facts and hypotheses," Intensive Care Med. **30**, 1865 (2004).
[6] J. W. Haft, B. P. Griffith, R. B. Hirschl, and R. H. Bartlett, "Results of an artificial-lung survey to lung transplant program directors," J. Heart Lung Transplant **21**, 467 (2002).
[7] J. B. Zwischenberger, C. M. Anderson, K. E. Cook, S. D. Lick, L. F. Mockros, and R. H. Bartlett, "Development of an implantable artificial lung: Challenges and progress," ASAIO J. **47**, 316 (2001).
[8] H. Sato, G. W. Griffith, C. M. Hall, J. M. Toomasian, R. B. Hirschl, R. H. Bartlett, and K. E. Cook, "Seven-day artificial lung testing in an in-parallel configuration," Ann. Thorac. Surg. **84**, 988 (2007).
[9] Y. Lin, D. O. Brant, R. H. Bartlett, R. B. Hirschl, and J. L. Bull, "Pulsatile flow past a cylinder: An experimental model of flow in an artificial lung," ASAIO J. **52**, 614 (2006).
[10] K. Chan, H. Fujioka, R. H. Bartlett, R. B. Hirschl, and J. B. Grotberg, "Pulsatile flow and mass transport over an array of cylinders: Gas transfer in a cardiac-driven artificial lung," J. Biomech. Eng. **128**, 85 (2006).
[11] J. R. Zierenberg, H. Fujioka, V. Suresh, R. H. Bartlett, R. B. Hirschl, and J. B. Grotberg, "Pulsatile flow and mass transport past a circular cylinder," Phys. Fluids **18**, 013102 (2006).
[12] J. R. Zierenberg, H. Fujioka, R. B. Hirschl, R. H. Bartlett, and J. B. Grotberg, "Pulsatile blood flow and oxygen transport past a circular cylinder," J. Biomech. Eng. **129**, 202 (2007).

[13]J. W. Haft, J. L. Bull, R. Rose, J. Katsra, J. B. Grotberg, R. H. Bartlett, and R. B. Hirschl, "Design of an artificial lung compliance chamber for pulmonary replacement," ASAIO J. **49**, 35 (2003).
[14]P. W. Bearman, "Vortex shedding from oscillating bluff bodies," Annu. Rev. Fluid Mech. **16**, 195 (1984).
[15]C. H. K. Williamson and R. Govardhan, "Vortex-induced vibrations," Annu. Rev. Fluid Mech. **36**, 413 (2004).
[16]H. M. Blackburn and R. D. Henderson, "A study of two-dimensional flow past an oscillating cylinder," J. Fluid Mech. **385**, 255 (1999).
[17]E. Guilmineau and P. Queutey, "A numerical simulation of vortex shedding from an oscillating circular cylinder," J. Fluids Struct. **16**, 773 (2002).
[18]T. Sarpkaya, "Structures of separation on a circular cylinder in periodic flow," J. Fluid Mech. **567**, 281 (2006).
[19]Y. D. Afanasyev and I. A. Filippov, "Formation of a vortex street behind and oscillating cylinder," Fluid Dyn. **30**, 40 (1995).
[20]I. Demirdžić and M. Perić, "Space conservation law in finite volume calculations of fluid flow," Int. J. Numer. Methods Fluids **8**, 1037 (1988).
[21]H. K. Versteeg and W. Malalasekera, *An Introduction to Computational Fluid Dynamics* (Longman Scientific and Technical, Essex, England, 1995).
[22]I. Demirdzic and S. Muzaferija, "Numerical method for coupled fluid flow, heat transfer and stress analysis using unstructured moving meshes with cells of arbitrary topology," Comput. Methods Appl. Mech. Eng. **125**, 235 (1995).
[23]S. V. Patankar and D. B. Spalding, "A calculation procedure for heat, mass and momentum transfer in three-dimensional parabolic flows," Int. J. Heat Mass Transfer **15**, 1787 (1972).
[24]I. Demirdžić, Ž. Lilek, and M. Perić, "A collocated finite volume method for predicting flows at all speeds," Int. J. Numer. Methods Fluids **16**, 1029 (1993).
[25]M. Perić and J. H. Ferziger, *Computational Fluid Dynamics*, 3rd ed. (Springer-Verlag, New York, 2002).
[26]S. F. Anwer, N. Hasan, S. Sanghi, and S. Mukherjee, "Computation of unsteady flows with moving boundaries using body fitted curvilinear moving grid," Comput. Struct. **87**, 691 (2009).
[27]J. F. Thompson, Z. U. A. Warsi, and W. C. Mastin, *Numerical Grid Generation: Foundation and Applications (ebook), High Performance Computing Collaboratory* (Mississippi State University, Mississippi, 1997).
[28]J. B. Wanderley and C. Levi, "Vortex induced loads on marine risers," Ocean Eng. **32**, 1281 (2005).
[29]C. H. K. Williamson, "Vortex dynamics in the cylinder wake," Annu. Rev. Fluid Mech. **28**, 477 (1996).
[30]S. Okamoto, R. Uematsu, and Y. Taguwa, "Fluid force acting on two-dimensional circular cylinder in lock-in phenomenon," JSME Int. J., Ser. B **45**, 850 (2002).